

**Mixed layer depth seasonality modulates summertime SST variability in the  
Southern Ocean**

Earle A. Wilson,<sup>a</sup> David B. Bonan,<sup>b</sup> Andrew F. Thompson,<sup>b</sup> Natalie Armstrong,<sup>c</sup> and Stephen  
C. Riser<sup>d</sup>

<sup>a</sup> *Department of Earth System Science, Stanford University, Stanford, CA, USA*

<sup>b</sup> *Environmental Science and Engineering, California Institute of Technology, Pasadena, CA, USA*

<sup>c</sup> *Department of Environmental Health and Engineering, Johns Hopkins University, Baltimore,  
MD, USA*

<sup>d</sup> *School of Oceanography, University of Washington, Seattle, WA, USA*

*Corresponding author:* Earle A. Wilson, earlew@stanford.edu

11 ABSTRACT: In recent years, the Southern Ocean has experienced unprecedented surface warming  
12 and sea ice loss—a stark reversal of sea ice expansion and surface cooling trends that prevailed  
13 over preceding decades. The most dramatic changes occurred in the austral spring of 2016  
14 when Antarctic sea-ice extent (SIE) reached a record minimum as sea surface temperatures (SST)  
15 climbed to a near-record high. In late 2019, another circumpolar surface warming event spanned  
16 the Southern Ocean, albeit with no appreciable decline in Antarctic SIE. A mixed layer heat budget  
17 analysis reveals that these recent circumpolar surface warming events were triggered by a weakening  
18 of the circumpolar westerlies, which decreased northward Ekman transport and accelerated the  
19 seasonal shoaling of the mixed layer. The latter effect amplified the surface warming effect of  
20 air-sea heat fluxes during months of peak solar insolation. More generally, summertime SST  
21 across the Southern Ocean is sensitive to the timing of the springtime shoaling of the mixed  
22 layer, which is controlled by the strength and temporal variance of the circumpolar westerlies. An  
23 examination of the CESM1 large ensemble demonstrates that these recent circumpolar warming  
24 events are consistent with the internal variability associated with the Southern Annual Mode  
25 (SAM), whereby negative SAM in austral spring favors shallower mixed layers and anomalously  
26 high summertime SST. Thus, future Southern Ocean surface warming extremes will depend on the  
27 evolution of regional mixed layer depths and interannual SAM variability.

28 SIGNIFICANCE STATEMENT: This study examines the physical mechanisms that can produce  
29 abrupt and extreme surface warming across the Southern Ocean. Using the unprecedented late  
30 2016 and 2019 Southern Ocean warming events as case studies, we demonstrate that the strength  
31 of the circumpolar westerlies in the spring strongly modulates regional sea surface temperatures  
32 (SSTs) in the summer. Weak circumpolar winds reduce the northward Ekman transport of cool  
33 subpolar waters and cause the mixed layer to shoal more rapidly in the spring. The latter effect traps  
34 more heat near the surface as the total air-sea heat flux to the ocean approaches its annual maximum.  
35 Further, we demonstrate that the unprecedented 2016 and 2019 Southern Ocean warming events are  
36 consistent with the internal variability associated with the Southern Annular Mode (SAM). These  
37 results suggest future Southern Ocean surface warming extremes will depend on the evolution of  
38 regional mixed layer depths and interannual SAM variability.

## 39 1. Introduction

40 The Southern Ocean has experienced exceptional sea ice decline and surface warming in recent  
41 years (Figure 1). During the austral spring of 2016, Antarctic sea ice retreated at an unusually rapid  
42 rate before reaching a record-low extent the following summer (Turner et al. 2017; Parkinson 2019;  
43 Eayrs et al. 2021). This anomalous sea ice decline coincided with widespread surface warming that  
44 extended beyond the Antarctic sea ice zone and culminated in record-high summertime sea surface  
45 temperatures (SSTs) (Stuecker et al. 2017; Meehl et al. 2019, Figure 1a). While Southern Ocean  
46 SSTs returned to normal after a few months, Antarctic sea-ice extent (SIE) remained exceptionally  
47 low over the next three years. In late 2019, the Southern Ocean experienced another abrupt  
48 circumpolar surface warming event of similar magnitude and spatial extent as the anomalous  
49 warming of late 2016, but there was no corresponding decline in Antarctic SIE (Figure 1b).

50 The extent to which these recent warming and sea ice loss anomalies reflect a shift in the  
51 Southern Ocean climate or transient manifestations of internal variability remains unclear. Over the  
52 preceding decades, the Southern Ocean experienced robust sea ice expansion and surface cooling  
53 that were near circumpolar in extent (Yuan and Martinson 2000; Cavalieri et al. 2003; Simmonds  
54 2015). The underlying drivers responsible for these longer timescale trends are uncertain; possible  
55 mechanisms include the strengthening of the circumpolar westerlies (Fan et al. 2014; Kostov et al.  
56 2017), increases in surface freshwater fluxes and stratification (Bintanja et al. 2013; Purich et al.

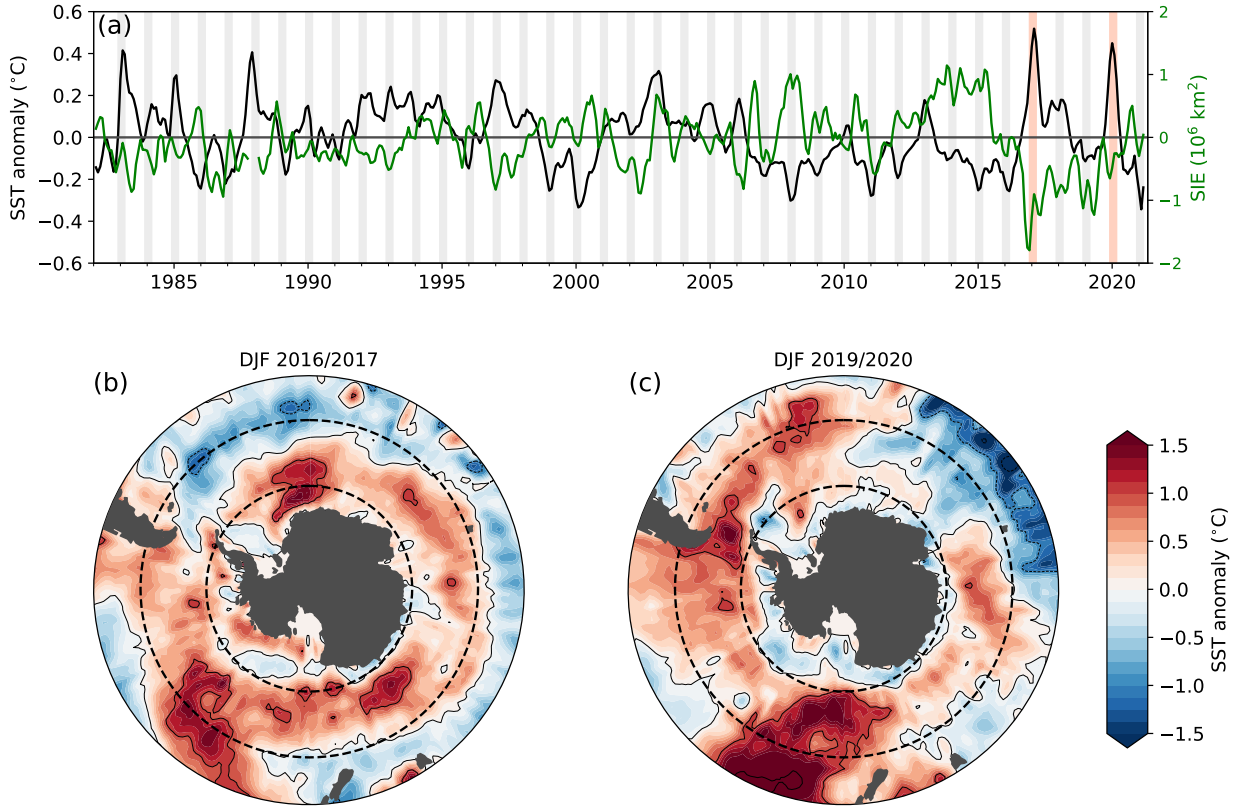


FIG. 1. (a) Temporal evolution of anomalous SST (black) and Antarctic SIE (green) in the Southern Ocean. (b, c) Seasonally averaged maps of anomalous SST during December–February (DJF) of 2016/2017 and 2019/2020. In (a), the vertical gray bars highlight austral summer (December–February). Dashed lines in (b) and (c) highlight 50°S–65°S, the latitudes over which the SST anomalies are spatially averaged in (a). Each time series has been smoothed with a 3-month rolling average.

2018; Haumann et al. 2020), atmospheric teleconnections from the tropical Pacific (Meehl et al. 2016; Li et al. 2021; Chung et al. 2022), and internal climate variability associated with Weddell Sea deep convection (Zhang et al. 2019). While it is certain that ongoing greenhouse emissions will eventually lead to sustained warming and sea ice loss across the Southern Ocean (Ferreira et al. 2015; Armour et al. 2016; Kostov et al. 2017), the timescale over which an anthropogenic signal will emerge above the noise of internal variability is poorly constrained (Doddridge et al. 2019; Rackow et al. 2022).

Previous studies suggest that the anomalous decline in Antarctic SIE that began in 2016 was due to multiple mechanisms operating over various timescales. This sea ice loss event has been linked



71 to anomalous variations in the Southern Annular Mode (SAM), El Niño–Southern Oscillation  
72 (ENSO), and Indian Ocean Dipole (IOD), which collectively weakened the circumpolar westerly  
73 jet and facilitated anomalous poleward advection of warm subtropical air into the subpolar region  
74 (Stuecker et al. 2017; Schlosser et al. 2018; Wang et al. 2019; Purich and England 2019). These  
75 mechanisms are distinct from the slower process of enhanced upwelling of warm Circumpolar  
76 Deep Water (CDW) that is expected to drive Southern Ocean sea ice loss and surface warming  
77 over the next century (Bitz and Polvani 2012; Ferreira et al. 2015). However, there is evidence that  
78 the gradual build-up of subsurface heat in the seasonal sea ice zone may have preconditioned some  
79 areas of the Southern Ocean for an unusually rapid springtime retreat of Antarctic sea ice (Meehl  
80 et al. 2019; Campbell et al. 2019).

81 It is likely that the mechanisms responsible for the recent decline in Antarctic sea ice are related  
82 but distinct from those that led to the recent circumpolar surface warming events. Though the  
83 2016 surface warming coincided with a steep loss in Antarctic sea ice, this was not the case  
84 in late 2019 (Figure 1a). Furthermore, previous circumpolar surface warming events, such as  
85 those that occurred during the austral spring and summers of 1982/1983 and 1987/1988, were not  
86 accompanied by an appreciable decrease in Antarctic SIE (Figure 1a). As with the late 2016 and  
87 2019 warming events, other prominent circumpolar warming events extended beyond the seasonal  
88 sea ice zone. Though previous studies have established links between Southern Ocean SST  
89 anomalies and the variance of SAM and ENSO (Sen Gupta and England 2006; Sallée et al. 2010;  
90 Ciasco and England 2011; Ding et al. 2012), there is no clear relationship between the intensity of  
91 SAM or ENSO phases and the magnitude of Southern Ocean SST anomalies. Thus, the particular  
92 set of circumstances that facilitated the extraordinary summertime SST anomalies in 2016/2017  
93 and 2019/2020 remain unclear. Since these surface warming events occur in spring and summer,  
94 they also provide a glimpse of the maximum SSTs that may occur across the Southern Ocean.  
95 Critically, circumpolar warming events may provide the basis for marine heatwaves (MHWs),  
96 which are more localized SST extremes that can lead to sharp declines in biodiversity and the  
97 collapse of ecosystems (Hobday et al. 2016; Frölicher et al. 2018; Holbrook et al. 2019; Smale  
98 et al. 2019; Oliver et al. 2021). Therefore, understanding the mechanisms that may lead to surface  
99 warming extremes is an essential step toward characterizing and predicting ecological sustainability  
100 in the Southern Ocean.

The primary purpose of this work is to elucidate the large-scale atmospheric and oceanic processes that give rise to extreme and abrupt circumpolar surface warming across the Southern Ocean. This work builds on previous analyses that have examined the seasonal evolution of Southern Ocean mixed layer temperature (MLT) (Dong et al. 2007, 2008; Tamsitt et al. 2016; Pellichero et al. 2017) by focusing on processes that can lead to severe surface warming. Likewise, our analysis extends previous work that has explored the Southern Ocean response to SAM and ENSO (Sen Gupta and England 2006; Sallée et al. 2010; Ciasto and England 2011) by explicitly examining how the seasonal phasing of these modes of climate variability can produce extreme summertime SSTs. In doing so, we assess the extent to which recent circumpolar surface warming anomalies can be explained by internal variability. A key result of this analysis is that variations in the seasonal phasing of mixed layer depth (MLD) and solar insolation during austral spring are a major source of interannual variability in Southern Ocean summertime SST. In particular, a sustained period of negative SAM in late austral spring, similar to what occurred in late 2016 and 2019, provides favorable conditions for abrupt and widespread surface warming anomalies across the Southern Ocean.

## 2. Data and Methods

### *a. Observations and reanalyses*

Monthly SST data were obtained from the NOAA Optimum Interpolation (OI) SST V2 product (Reynolds et al. 2002), while subsurface temperature and salinity variability are assessed from the Argo-based Roemmich-Gilson climatology (Roemmich and Gilson 2009). Estimates of Antarctic sea ice concentration (SIC) were retrieved from the NOAA/NSIDC Climate Data Record (CDR) of SIC (Meier et al. 2013). SIE is defined as the area over which SIC is greater than 15%. Estimates of surface wind stress, sea level pressure, and air-sea heat fluxes were sourced from the ECMWF monthly ERA5 global atmospheric reanalysis (Hersbach et al. 2020). The reanalysis estimates were regridded from a  $0.25^\circ$  by  $0.25^\circ$  horizontal grid to a coarser  $1^\circ$  by  $1^\circ$  horizontal grid using a bi-linear interpolation scheme, consistent with the RG Argo and the NOAA OI SST data products.

While the SST data and atmospheric reanalysis products are analyzed for 1982–2020, the mixed layer heat budget analysis is carried out for the 2004–2020 period when subsurface Argo data are available. The depth of the mixed layer is defined using a density threshold of  $0.03 \text{ kg m}^{-3}$  (de

130 Boyer Montégut et al. 2004). The SAM index is defined as the zonal-mean sea level pressure  
131 difference between 65°S and 40°S (Marshall 2003). ENSO variability is quantified using the  
132 Niño3.4 index, which describes the area-averaged SST anomaly between 170°W–120°W and  
133 5°S–5°N. The SAM and Niño3.4 indices are normalized by their respective standard deviations.  
134 Anomalies are computed relative to a monthly averaged climatology. For the SST and reanalysis  
135 data, the climatological reference period is 1982–2015, while for the Argo data, the climatological  
136 reference period is 2004–2015.

137 To contextualize recent abrupt circumpolar warming events, observations are compared with  
138 output from the Community Earth System Model Version 1 Large Ensemble (CESM1-LE) (Kay  
139 et al. 2015). The CESM1-LE is a state-of-the-art fully coupled, 1° horizontal resolution 40-member  
140 initial condition ensemble, where each ensemble member is subjected to identical historical and  
141 RCP8.5 external forcing scenarios. However, each member differs slightly in the initial atmospheric  
142 state, producing a representation of internal variability across ensemble members, in the presence  
143 of forced climate change. We focus on the 1980–2020 period that overlaps with the modern satellite  
144 record.

#### 145 *b. Southern Ocean mixed layer heat budget*

146 Physical controls on Southern Ocean SST are evaluated using a mixed layer heat budget. In  
147 this study, MLT and SST are assumed to be equivalent. The heat budget is constructed for the  
148 mostly ice-free latitude band of 50°–65°S, which envelops the core of the circumpolar westerly jet  
149 and much of the Antarctic Circumpolar Current (ACC). Importantly, this is the latitudinal band  
150 over which zonally averaged SST anomalies are cool (warm) in response to a positive (negative)  
151 SAM phase (Sen Gupta and England 2006). Further north, between 30°S–50°S, the SST response  
152 to SAM is reversed. This analysis focuses on the 50°–65°S circumpolar band, over which the  
153 anomalous warming events of late 2016 and 2019 were most apparent (see Figure 1b-c).

154 As demonstrated by Dong et al. (2007), domain-averaged variations in MLT  $T_m$  across the  
155 circumpolar channel is primarily governed by heating due to air-sea fluxes, northward Ekman

transport, and wind-driven entrainment. This balance is given by

$$\frac{1}{A_s} \iint \frac{\partial T_m}{\partial t} dA \approx \frac{1}{A_s} \iint \left( \frac{Q_{ao}}{\rho_0 c_w h_m} - v_{Ek} \frac{\partial T_m}{\partial y} - w_{ent} \frac{\Delta T}{h_m} \right) dA, \quad (1)$$

$$\frac{1}{A_s} \iint \dot{T}_m dA \approx \frac{1}{A_s} \iint (\dot{T}_{ao} - \dot{T}_{Ek} - \dot{T}_{ent}) dA, \quad (2)$$

$$\dot{\bar{T}}_m \approx \dot{\bar{T}}_{ao} - \dot{\bar{T}}_{Ek} - \dot{\bar{T}}_{ent}, \quad (3)$$

where  $Q_{ao}$  is the net air-sea heat flux comprised of the sum of radiative and turbulent heat fluxes,  $v_{Ek}$  is the meridional Ekman velocity,  $\Delta T$  is the temperature difference between the mixed layer and just below the mixed layer,  $h_m$  is the mixed layer depth,  $w_{ent} = \dot{h}_m$  is the entrainment rate, and  $A_s$  is the surface area of the circumpolar control volume. The meridional Ekman velocity is given by  $v_{Ek} = \tau^x / (\rho_0 f h_m)$ , where  $\tau^x$  is the zonal component of the surface wind stress,  $\rho_0 = 1025 \text{ kg m}^{-3}$  is a reference seawater density, and  $f \approx 10^{-4} \text{ s}^{-1}$  is the Coriolis parameter. Following the procedure outlined in Dong et al. (2007),  $Q_{ao}$  is modified slightly to account for the fraction of shortwave radiation that is transmitted through the base of the mixed layer.

Equation (3) is valid when evaluating the heat balance over the entire circumpolar channel. Over smaller spatial scales, geostrophic transport and eddy mixing, which are neglected in this framework, have leading-order impacts on surface temperature variability (Tamsitt et al. 2016; du Plessis et al. 2022; Gao et al. 2022). It is also assumed that meridional eddy fluxes across the northern and southern boundaries of the control volume make small contributions to the domain-averaged MLT tendency  $\dot{\bar{T}}_m$  on monthly timescales. Though it is relatively straight-forward to evaluate  $\dot{\bar{T}}_{ao}$  and  $\dot{\bar{T}}_{Ek}$  from Argo data and atmospheric reanalysis,  $\dot{\bar{T}}_{ent}$  presents a greater challenge since it is influenced by sub-monthly variations in  $h_m$  that are not well-resolved by the current Argo observing array (Carranza and Gille 2015). Therefore, the effect of vertical entrainment is estimated from the residual of the other heat budget terms.

### 3. Results

#### *a. Climate conditions during recent circumpolar warming events*

During the austral spring of 2016 and 2019, the domain-averaged surface buoyancy fluxes across the Southern Ocean were not consistently different from the climatological mean (Figure 2a).

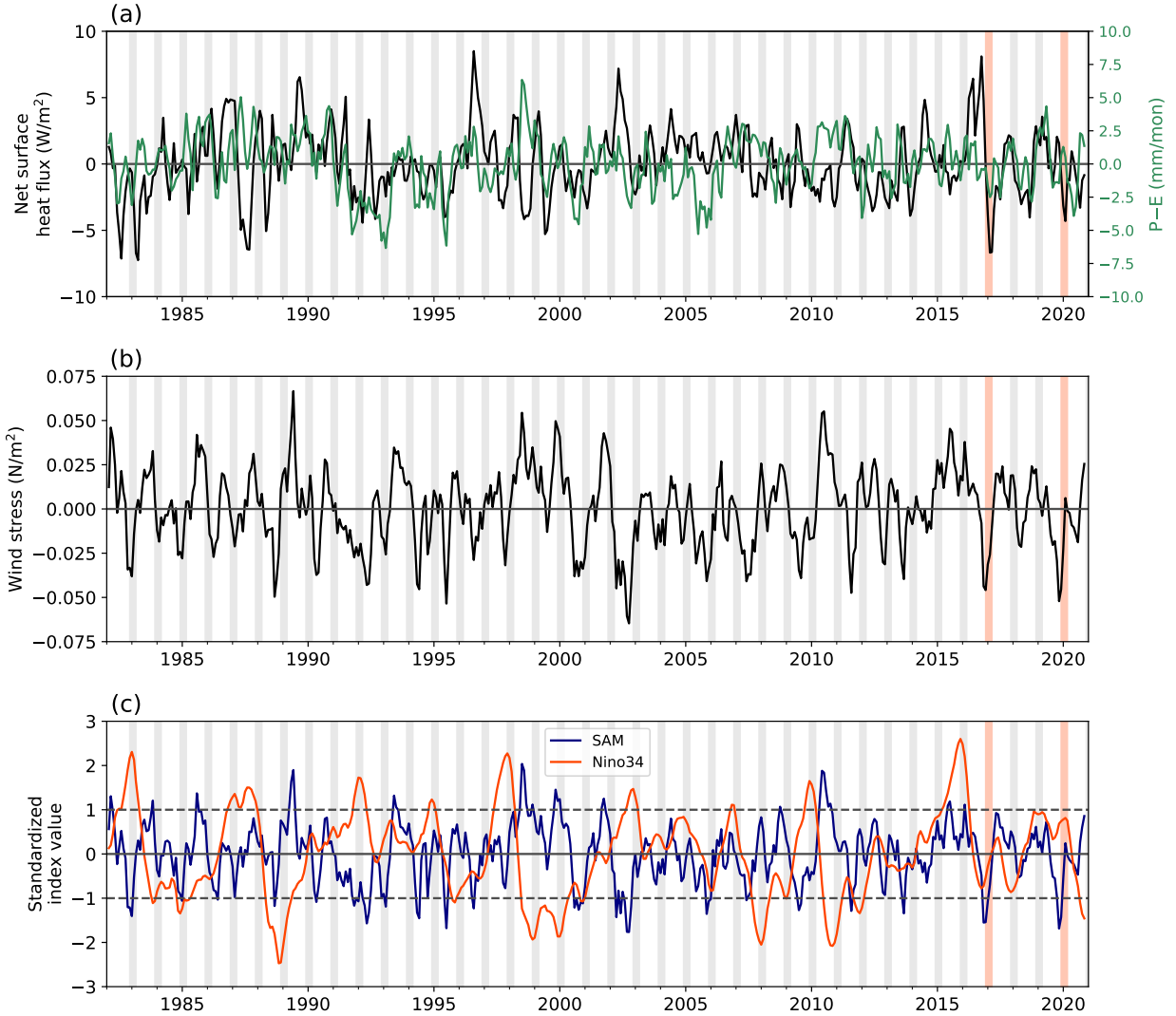


FIG. 2. (a) Domain-averaged net surface heat flux anomalies (black) and precipitation minus evaporation anomalies ( $P-E$ , green) across  $50^{\circ}\text{S}$ – $65^{\circ}\text{S}$ . Positive air-sea heat fluxes signify ocean heat gain. (b) As in (a) but showing zonal wind stress anomalies. (c) Temporal evolution of the SAM (blue) and the Nino3.4 indices (orange). Vertical gray bars highlight austral summer (December–February). The linear trend has been removed from each time series, and temporal variations are smoothed using a 3-month rolling average.

Though the late 2016 warming event followed unusually warm winter and spring, this was not the case in 2019. Additionally, the spatial patterns of anomalous air-sea fluxes were not consistent with the patterns of anomalous warming during both circumpolar warming events (Figure 3). While in some instances, patterns of anomalously high air-sea heating and mixed layer warming overlapped,

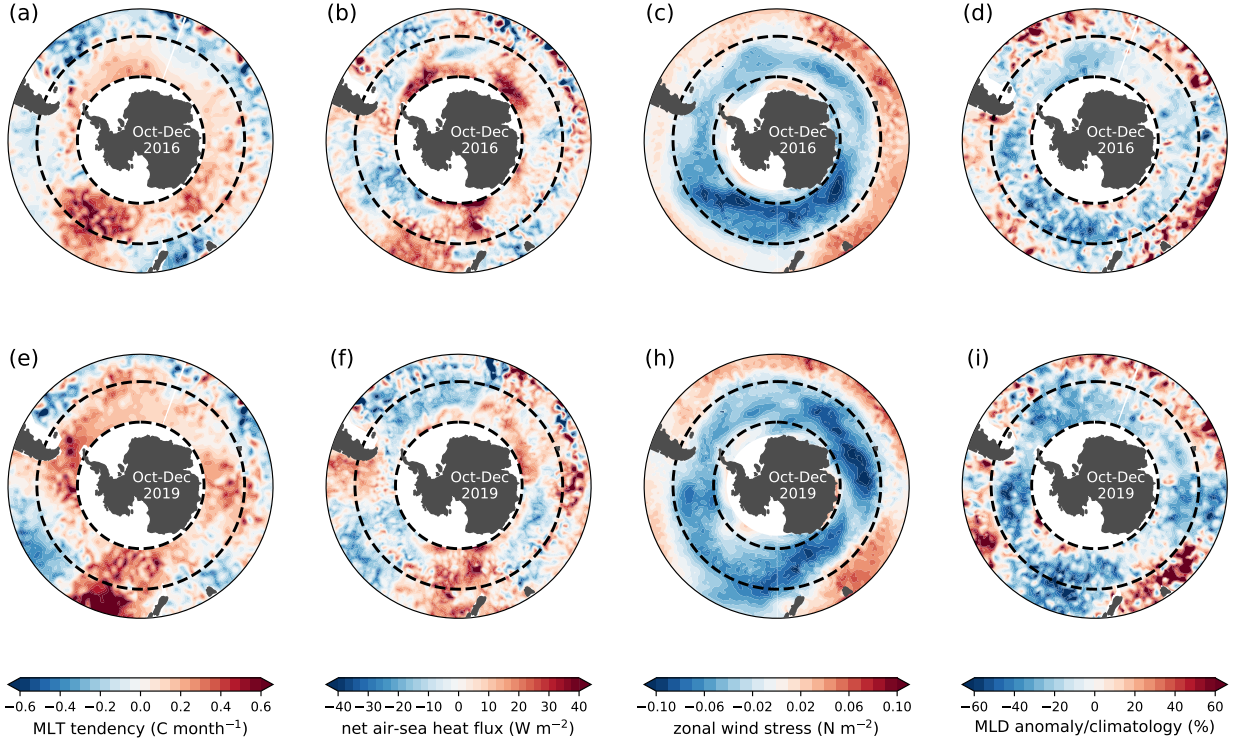


FIG. 3. Southern Ocean surface conditions during October–December of 2016 (top row) and 2019 (bottom row): (a, e) MLT tendency anomalies, (b, f) Net air-sea heat flux anomalies, (c, h) zonal wind stress anomalies, and (d, i) MLD anomalies as percentages of the monthly climatological means. Black dashed lines outline the circumpolar channel (50°S–65°S over which the mixed layer heat budget is evaluated).

this was often not the case. For example, during October–December of 2019, air-sea heat fluxes across the southern Atlantic favored anomalous surface cooling while the mixed layer warmed at an accelerated rate (Figure 3e,f). Thus, the recent circumpolar warming events cannot be directly attributed to anomalous air-sea heat fluxes.

On the other hand, circumpolar westerlies were extraordinarily weak in late 2016 and 2019, with zonally averaged surface wind stress anomalies exceeding  $-0.04 \text{ N m}^{-2}$  (Figure 2b)—a  $\sim 30\%$  reduction relative to the climatological mean. During both warming events, the collapse of the surface westerlies spanned all longitudes (Figure 3 c, h). Concurrently, there was widespread anomalous MLD shoaling across the Southern Ocean (Figure 3d,f). The anomalous shoaling was most striking in late 2019 when the MLD across the circumpolar channel was, on average, roughly

206 20% shallower than usual. The late 2016 and 2019 anomalous shoaling events did not coincide  
207 with increased surface heat or freshwater fluxes (Figure 2a).

208 Consistent with the strong reduction in circumpolar westerly winds, SAM was in an exceptionally  
209 negative phase during both circumpolar warming events. In both cases, the SAM index was roughly  
210 1.5 standard deviations below its annual mean value (Figure 2b). ENSO was in a relatively neutral  
211 state during these periods, tending towards its La Niña and El Niño phases during the austral spring  
212 of 2016 and 2019, respectively.

### 213 *b. Drivers of anomalous mixed layer warming in late 2016 and 2019*

219 Evaluating the circumpolar mixed layer heat budget (Equation 3) reveals that the heating anoma-  
220 lies associated with air-sea heat fluxes  $\dot{\bar{T}}_{ao}$  and northward Ekman transport  $\dot{\bar{T}}_{Ek}$  were the primary  
221 drivers of the anomalous surface warming in late 2016 and 2019 (Figure 4). In late 2016,  $\dot{\bar{T}}_{Ek}$   
222 anomalies peaked at roughly  $0.08\text{ }^{\circ}\text{C month}^{-1}$ , which was slightly less than the overall mixed layer  
223 warming of  $0.1\text{ }^{\circ}\text{C month}^{-1}$  (Figure 4b). In late 2019, anomalies in  $\dot{\bar{T}}_{Ek}$  accounted for roughly  
224 half of the observed mixed layer warming. The decrease in Ekman-driven cooling is consistent  
225 with the anomalously weak zonal wind stress during these periods (Figure 3c,h). The enhancement  
226 of  $\dot{\bar{T}}_{ao}$  was largely due to anomalous MLD shoaling. Thus, even though air-sea heat fluxes were  
227 not substantially different from the climatological mean during the warming events, their effect on  
228 MLT was greatly amplified.

229 Estimating  $\dot{\bar{T}}_{ent}$  as a residual of Equation (3) suggests that entrainment-driven mixed layer cooling  
230 was enhanced during late 2016 and 2019 (Figure 4b). This implied amplification of  $\dot{\bar{T}}_{ent}$  under  
231 weaker surface winds reveals a complex interplay between wind-driven mixing, MLD, and the  
232 variance of surface winds. Since  $\dot{\bar{T}}_{ent}$  is dependent on MLD and the temperature gradient below  
233 the mixed layer (Eq. 3), this term does not necessarily scale with the amplitude of the surface wind  
234 stress. Moreover, the temperature of a shallower mixed layer will be more sensitive to the mixing  
235 generated by episodic storms and strong wind events. Nevertheless, without direct estimates of  
236 entrainment-driving mixing, the contribution of  $\dot{\bar{T}}_{ent}$  is not well constrained.

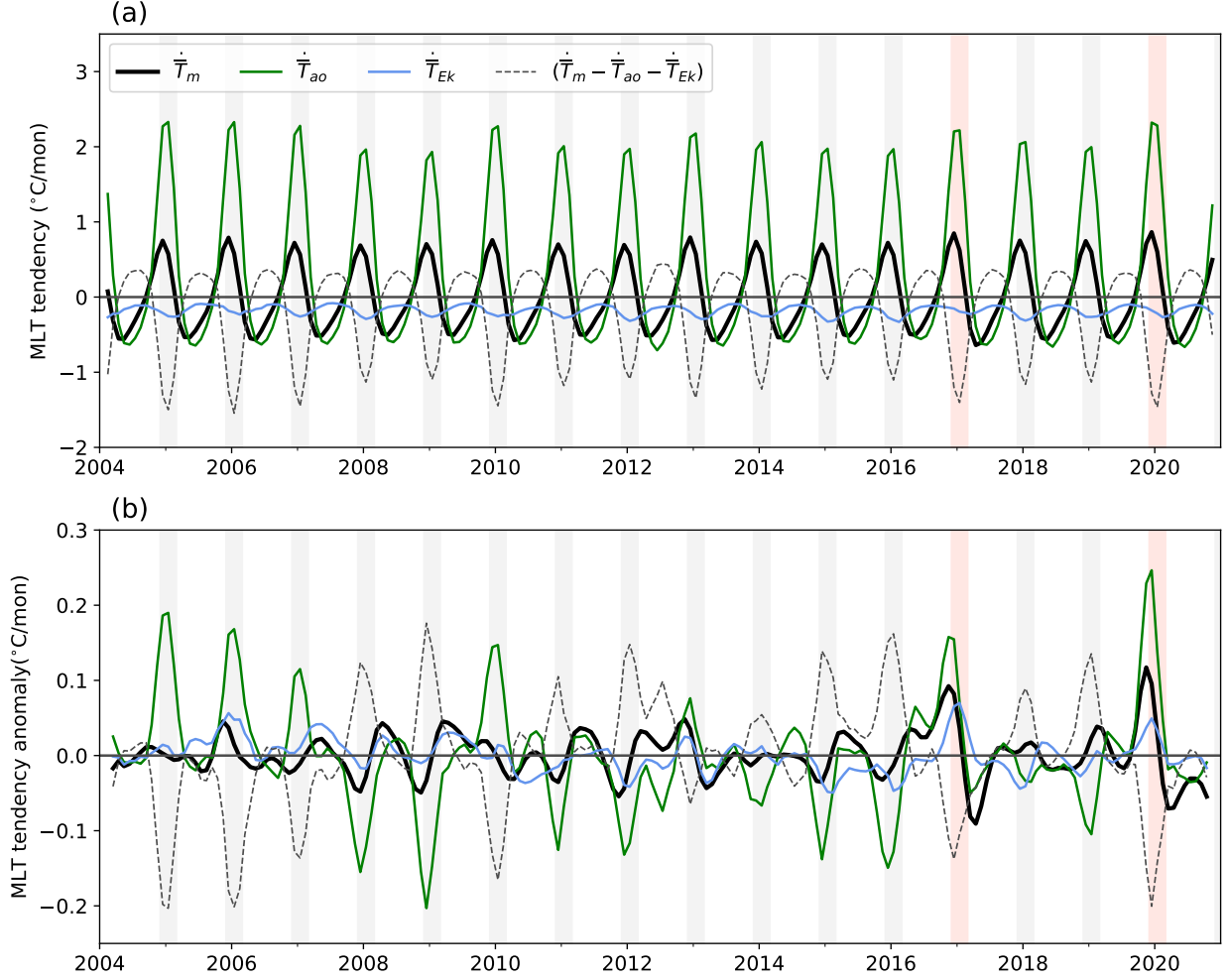


FIG. 4. Evolution of the Southern Ocean mixed layer heat budget, described by Eq. (3). (a) Monthly tendencies in MLT (black) due to air-sea heat fluxes (green) and meridional Ekman transport (blue). The gray dashed line represents the residual of the heat budget ( $\dot{T}_m - \dot{T}_{ao} - \dot{T}_{Ek}$ ), which is interpreted as the component due to entrainment. (b) As in (a) but after removing the monthly climatology. Gray vertical bars highlight December–February.

### c. The seasonal phasing of mixed layer depth and air-sea heat fluxes

The seasonal evolution of  $\dot{T}_m$  is re-examined in the phase-space defined by  $h_m$  and  $Q_{ao}$  (Figure 5). Since the seasonal variation of  $\tau^x$  is small compared to that of MLD and  $Q_{ao}$ , we focus on the sum of the mixed layer warming due to northward Ekman transport and air-sea heat fluxes,  $\dot{T}_{ao+Ek} \equiv \dot{T}_{ao} + \dot{T}_{Ek}$ , assuming a constant surface wind stress of  $\tau^x = 0.15 \text{ N m}^{-2}$ . During the cooling season (March–September),  $\dot{T}_{ao}$  and  $\dot{T}_{Ek}$  combine to cool the relatively deep mixed layer



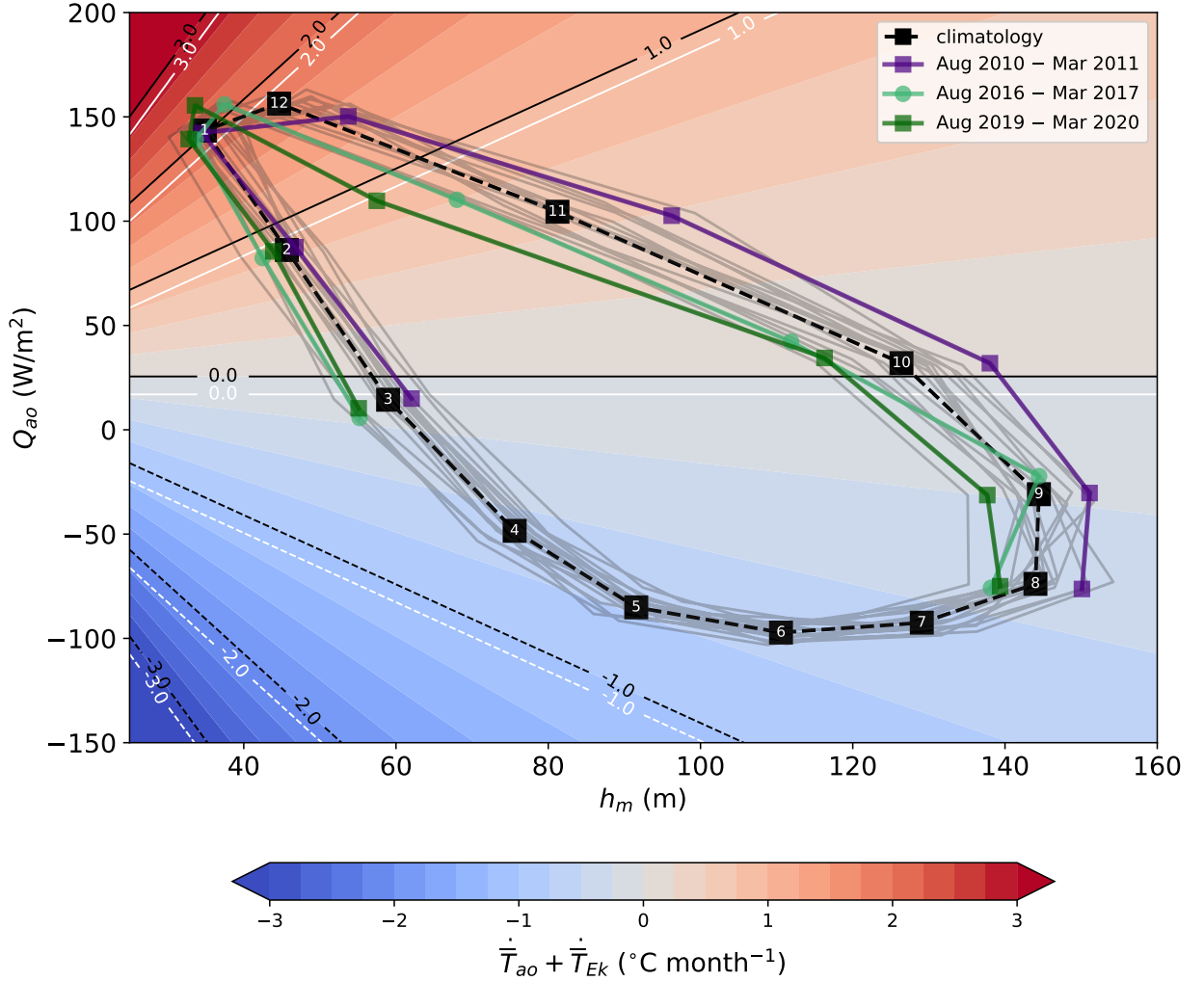


FIG. 5. Phase diagram showing the relationship between seasonal variations in mixed layer depth  $h_m$ , air-sea heat fluxes  $Q_{ao}$ , and mixed layer temperature tendency due to the sum of air-sea heating  $\dot{\bar{T}}_{ao}$  and Ekman transport  $\dot{\bar{T}}_{Ek}$  (contours and shading). Gray lines represent seasonal trajectories from 2004–2020, while the dashed black line represents the climatological mean. For the latter, the numbering of the black squares signifies the calendar month. The purple and green lines highlight trajectories between August–March for 2015/2016, 2016/2017, and 2019/2020, respectively. For the background shading and black contours, the heating associated with northward Ekman transport  $\dot{\bar{T}}_{Ek}$  is computed assuming a typical value of  $\tau^x = 0.15 \text{ N m}^{-2}$ . White contours show  $\dot{\bar{T}}_{ao} + \dot{\bar{T}}_{Ek}$  for the case where  $\tau^x = 0.1 \text{ N m}^{-2}$ .

at a peak rate of approximately  $0.75^\circ\text{C month}^{-1}$ . During the warming season (October–February),  $\dot{\bar{T}}_{ao+Ek}$  provides a surface warming that reaches a maximum of  $\sim 2^\circ\text{C month}^{-1}$  between January and February. The seasonal asymmetry of  $\dot{\bar{T}}_{ao+Ek}$  arises from the nonlinear dependence of  $\dot{\bar{T}}_{ao}$  on  $h_m$ .

As  $h_m$  approaches its summertime minimum,  $\dot{\bar{T}}_{ao+Ek}$  becomes increasingly sensitive to variations in  $h_m$  and  $Q_{ao}$ , with  $\dot{\bar{T}}_m$  being more sensitive to periods of anomalous mixed layer shoaling than anomalous deepening. The effect of  $\dot{\bar{T}}_{Ek}$  may be discerned by the offset in the position of the  $\dot{\bar{T}}_{ao+Ek} = 0$  contour in Figure 5. In the limit of no surface heating  $Q_{ao} \rightarrow 0$ , only northward Ekman transport contributes to heating.

In the phase-space defined by  $h_m$  and  $Q_{ao}$ , the impact of the extraordinary MLD shoaling in late 2016 and 2019 is immediately evident. During these anomalous warming periods (green lines in Figure 5), the Southern Ocean mixed layer followed a relatively shallow trajectory in the  $Q_{ao}-h_m$  phase space, which accelerated the springtime warming of the mixed layer. In most years,  $Q_{ao}$  reaches a maximum amplitude of  $\sim 150 \text{ W m}^{-2}$  in December, one month before  $h_m$  reaches its minimum value of  $\sim 40 \text{ m}$ . In late 2016 and 2019, the seasonal  $h_m$  minimum occurred approximately one month earlier than usual, coinciding with maximal air-sea heat fluxes. This shoaling-induced mixed layer warming anomaly was most apparent in November of 2019 when  $h_m$  was 20–30 m shallower than the climatological mean—a record low for the Argo period. The enhanced mixed layer warming due to  $\dot{\bar{T}}_{ao}$  is augmented by a reduction in the cooling provided by  $\dot{\bar{T}}_{Ek}$ , which equates to a downward translation of the  $\dot{\bar{T}}_{ao+Ek}$  pattern in Figure 5. The accelerated mixed layer warming of late 2016 and 2019, which occurred during strong negative SAM events, is contrasted with the more gradual warming that occurred in late 2010 (purple line in Figure 5), a period characterized by positive SAM conditions (Figure 2b,c). In the latter scenario, the anomalously deep Southern Ocean mixed layer warmed at a relatively slow rate, leading to anomalously cool summertime surface temperatures (Figure 1a).

#### *d. Sensitivity of mixed layer warming to the timing of surface wind anomalies*

The preceding analyses suggest that anomalous mixed layer shoaling and warming during the austral spring of 2016 and 2019 were initiated by a weakening of the circumpolar westerlies. To quantify the springtime sensitivity of MLD and MLT to surface wind variability, a set of idealized simulations were conducted using a one-dimensional ocean mixing model (Appendix A1). The Kraus-Turner mixed layer model was forced with idealized surface fluxes of buoyancy and momentum that mimic observations across  $50^\circ\text{S}$ – $65^\circ\text{S}$  during October and February (late spring through summer). For the wind stress forcing, we employ synthetic surface winds that are

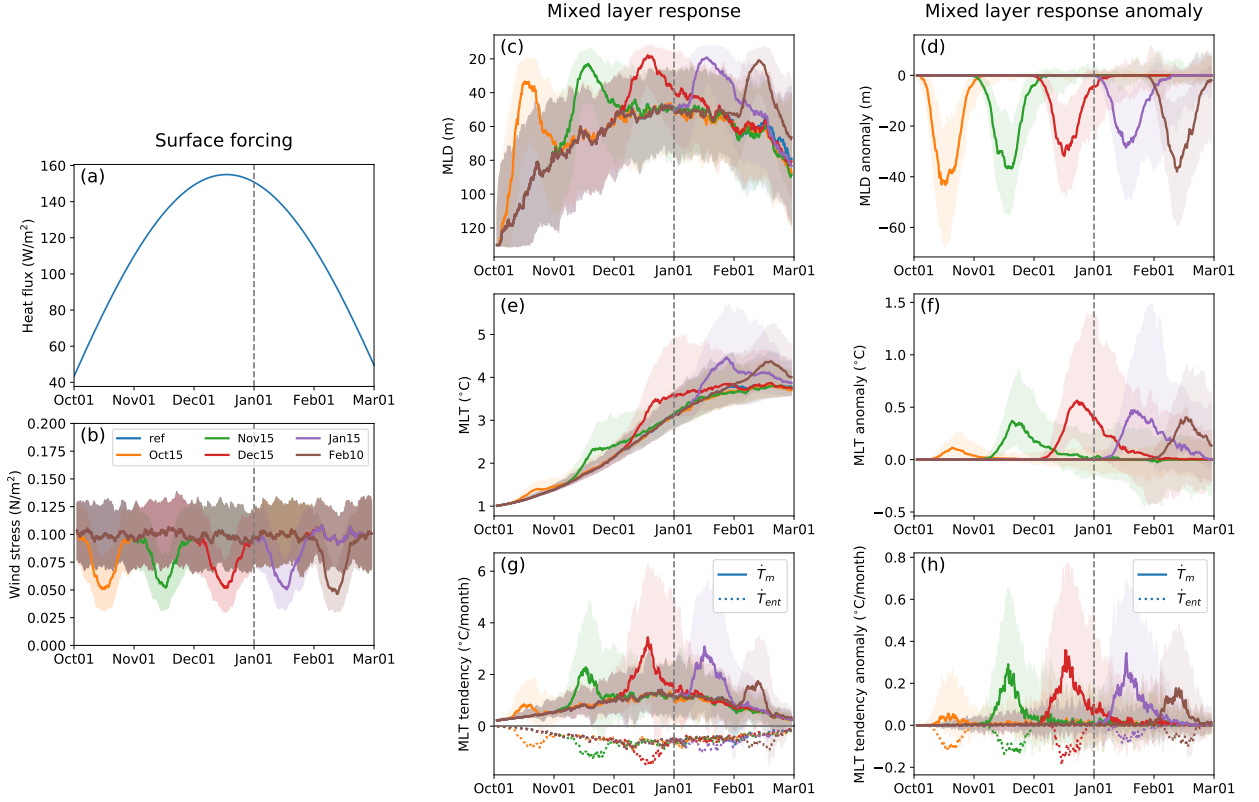


FIG. 6. Results from the idealized 1D mixing experiments. (a) The prescribed surface heat fluxes used in all experiments. (b) The synthetically generated surface wind stress used in the reference and perturbation experiments, where for the latter set a Gaussian filter was used to dampen the winds by a maximum of 50% over five different periods. Middle column shows the MLD (c), MLT (e) and MLT tendency (g) responses. The right column (d, f, h) shows the mixed layer response anomalies relative to the reference case with no wind perturbation. Each experiment consists of 200 ensemble members forced by a unique wind time series constructed from a red noise spectrum. The shading represents the interquartile range, and solid lines represent the median response. In (g, h), dotted lines represent mixed layer temperature tendency associated with entrainment  $\dot{T}_{ent}$ . The interquartile range for  $\dot{T}_{ent}$  is omitted for clarity. See Appendix A1 for further details.

generated from a red-noise spectrum and have a time-mean magnitude of  $0.1 \text{ N m}^{-2}$ . For a single experiment, we conducted 200 simulations, each with a unique surface wind forcing.

For the reference case, the mixed layer gradually shoals and warms between October and February, reaching a minimum depth of roughly 50 m and a maximum temperature of approximately  $4^\circ\text{C}$ , which are consistent with observations (Figure 6). In the perturbation experiments, a Gaussian kernel is used to reduce the time-mean wind stress magnitude by a maximum value of 50% over

various 10-day windows. The time-mean wind strength is reduced during the perturbation period without modifying the temporal variance.

Reducing the strength of the winds increases the rate at which the mixed layer shoals and warms. The amplitude of the MLD shoaling is not sensitive to the timing of the wind anomaly, with the median response ranging between 30–40 m. In contrast, the amplitude of mixed layer warming varies substantially with the timing of the wind perturbation. The median MLT anomaly ranges from 0.1 °C when the wind perturbation is applied in mid-October to 0.5 °C when the winds are reduced by an equivalent amount in mid-December. The latter warming anomaly occurs when the MLD and surface heat fluxes are at their respective minimum and maximum.

In the perturbation experiments, weaker winds lead to an increase in entrainment-driven mixed layer cooling  $\dot{T}_{ent}$ , which is consistent with what is inferred from observations in late 2016 and 2019 (Figure 4). However, the simulated response of  $\dot{T}_{ent}$  is sensitive to the temporal variance of the surface winds. In experiments where the temporal variance is reduced in a similar manner as the temporal mean, the change in  $\dot{T}_{ent}$  is negligible (not shown). These results indicate that wind-driven entrainment is strongly controlled by the temporal variance of the wind stress amplitude, with high-wind extremes having a disproportionate impact on entrainment.

Additional simulations (not shown here) were conducted to evaluate the sensitivity of the mixed layer responses to the duration and sign of the wind perturbation. Prolonging the weakening of the winds leads to equivalent changes in the MLD and heating tendency anomalies, with the extended accumulation of  $\dot{T}$  anomalies resulting in a larger absolute change in MLT. Applying a positive wind perturbation produces a response opposite to the case with weaker winds, albeit with more minor MLT anomalies due to the deeper mixed layers.

Though idealized, these numerical simulations demonstrate that a reduction in wind-driven mixing can generate MLT anomalies similar in magnitude to those observed during the austral spring and summer of 2016/2017 and 2019/2020. The decrease in northward Ekman transport, a process not included in our idealized model, would further augment the surface warming response.

#### *e. Role of internal climate variability*

Given the rarity of these abrupt circumpolar warming events and our short observational record, we examine output from the 40-member CESM1-LE to gain a more robust understanding of

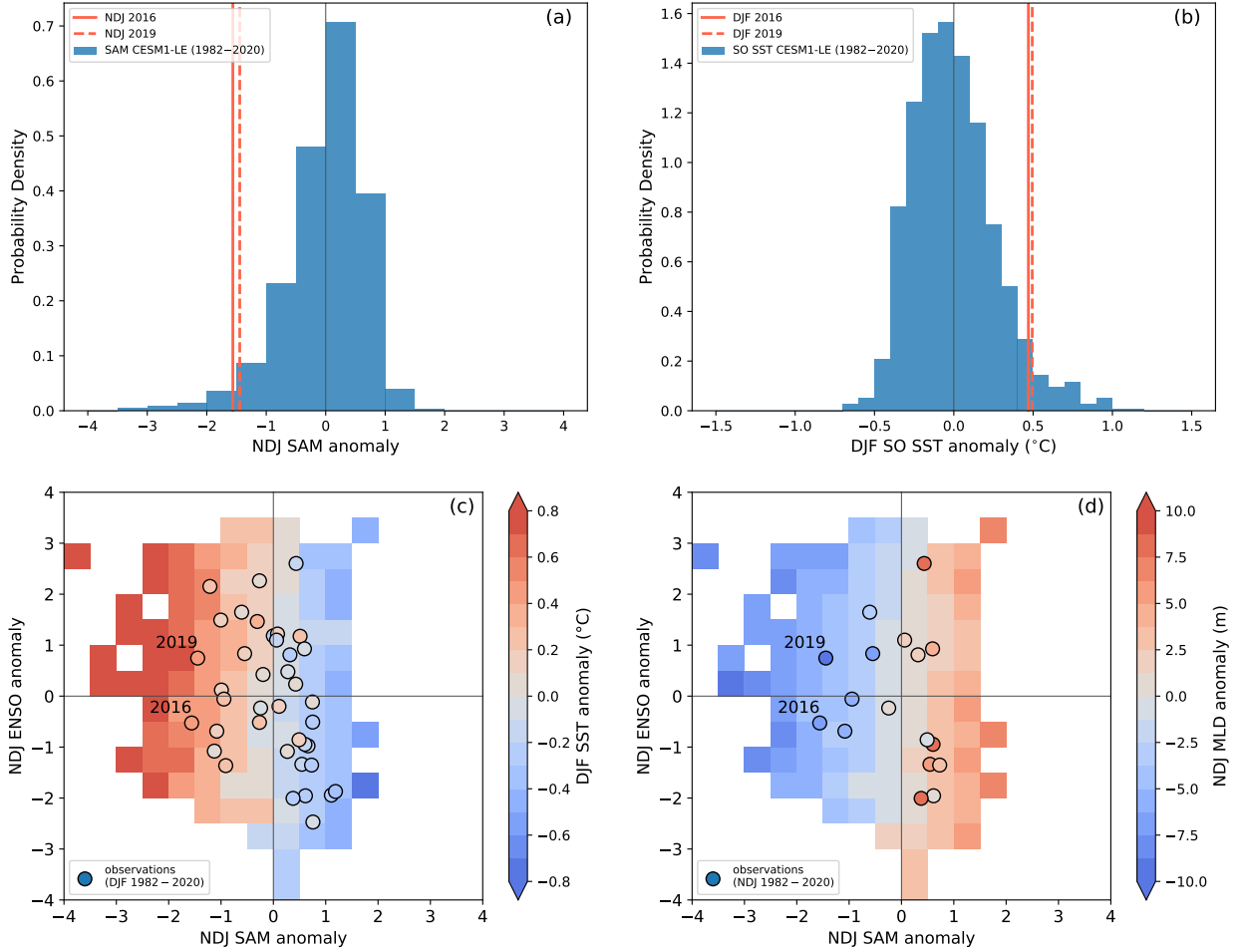


FIG. 7. Comparisons of SAM and Southern Ocean SST variability in the 40-member CESM1-LE with observations during 1982–2020. (a) Probability density distribution of the November–January (NDJ) SAM index in the CESM1-LE. (b) As in (a), but for domain-averaged DJF Southern Ocean SST anomalies across 50°–65°S. (c) Composites of domain-averaged DJF Southern Ocean SST anomalies in relation to NDJ SAM and ENSO. (d) As in (c), but showing NDJ Southern MLD anomalies. For the CESM1-LE results, anomalies refer to deviations from the ensemble mean. In (a) and (b), the frequency distributions of SAM and Southern Ocean SST are generated using 0.5 standard deviations and 0.1°C bins, respectively. For the observed seasonal averages shown here, the listed year represents the year the season begins.

these phenomena. Specifically, we investigate the response of summertime Southern Ocean SST (December–February; DJF) to variations of SAM in the preceding austral spring. An observational analysis of the lead-lag relationship between the SAM index and DJF SST across 50°–65°S shows that maximal correlation ( $r \approx -0.75$ ) is attained when SST is lagged by one month. Therefore,

we assess the relationship between Southern Ocean SST anomalies in DJF with SAM variability in November–January (NDJ) in the CESM1-LE. To isolate the effect of internal variability, we evaluate the variance of SAM and Southern Ocean SST after removing the ensemble-mean values, which represent the responses to anthropogenic forcing.

Though rare, Southern Ocean climate extremes like those observed in late 2016 and 2019 appear in the CESM1-LE (Figure 7a,b). In the CESM1-LE, NDJ periods where the SAM index is more than 1.5 standard deviations below average occur roughly once every 20 years. The distribution of NDJ SAM events also has a notable skew towards negative SAM events (Figure 7a). Importantly, the simulated Southern Ocean SST and MLD responses to late-spring SAM variability are consistent with observations. In particular, the mixed layer warming and shoaling observed in late 2016 and 2019 are consistent with equivalent events in the CESM1-LE (Figure 7c, d). To quantify the relative effect of SAM and ENSO in the CESM1-LE, we create composites of Southern Ocean SST and MLD anomalies using 0.5 standard deviation bins. In the CESM1-LE, strong SAM and ENSO events can occur independently, and it is evident that SAM has the dominant control over domain-averaged SST and MLD anomalies across 50°S–65°S. The sensitivity of summertime Southern Ocean SST and MLD to SAM variability is less apparent for individual ensemble members, and a strong dependence on SAM only emerges after averaging anomalies across the 40-member ensemble. These results indicate that other modes of variability significantly impact interannual variations of Southern Ocean SST and MLD in austral spring.

#### 4. Discussion

This study demonstrates that the relative seasonal phasing of MLD shoaling and air-sea heat fluxes is a key driver of interannual variability in summertime Southern Ocean SST. Between September and December, the zonally averaged MLD between 50°S–65°S shoals from its winter maximum of ~150 m to its summer minimum of ~50 m (Fig. 5). The rate at which this shoaling occurs varies substantially from year to year and produces an equivalently large spread in the rate at which the mixed layer warms. In the austral spring of 2016 and 2019, the Southern Ocean mixed layer shoaled at the fastest rates observed during the Argo era, which amplified the warming effect of solar insolation when it was near its seasonal maximum. During both events, the anomalous MLD shoaling was initiated by a dramatic weakening of the circumpolar westerlies associated

368 with strong negative SAM events. The weaker westerlies also reduced northward Ekman transport,  
369 further amplifying the mixed layer warming.

370 While several studies have shown that SAM has substantial control over springtime MLD and  
371 MLT (e.g., Sen Gupta and England 2006; Sallée et al. 2010), this study quantifies the high degree  
372 to which mixed layer warming is sensitive to the timing of the SAM anomalies. In particular,  
373 a sustained negative SAM event in November is expected to yield surface warming anomalies  
374 that are at least twice that produced by a similar SAM event occurring one month earlier. The  
375 late 2016 and 2019 warming events followed intense periods of negative SAM, which peaked  
376 during November and December, during which the MLT response to surface wind variability was  
377 maximal. This temporal sensitivity may explain why the negative SAM event in late 2002 did not  
378 lead to anomalous surface warming as severe as what was observed in late 2016 and 2019 (Figs.  
379 1a, 2c). Though the late 2002 negative SAM event was just as intense and more prolonged than the  
380 2016 and 2019 SAM events, the former peaked in October before transitioning to a more neutral  
381 state in November.

382 Abrupt circumpolar surface warming events, such as those observed across the Southern Ocean  
383 in late 2016 and 2019, occur in the CESM1-LE. These events are relatively rare, occurring roughly  
384 every 20 years in the CESM1-LE. Additionally, the Southern Ocean SST and MLD response  
385 to SAM in the CESM1-LE aligns well with recent observations. The CESM1-LE also features  
386 springtime negative SAM events that are more extreme than what has been observed over the past  
387 four decades, which suggests that the SAM variability may drive even more intense summertime  
388 surface warming anomalies in the future. In the CESM1-LE, SAM has a much stronger influence on  
389 zonally averaged summertime SST variability across the circumpolar channel than ENSO. However,  
390 examining individual ensemble members reveals that ENSO and other modes of variability can  
391 substantially modulate summertime Southern Ocean SST variability in a given year. Nevertheless,  
392 we conclude that the anomalous circumpolar warming of late 2016 and 2019 were primarily  
393 manifestations of internal climate variability. This assessment is in agreement with previous  
394 analyses that examine mechanisms responsible for recent declines in Antarctic SIE (e.g., Stuecker  
395 et al. 2017; Eayrs et al. 2021).

396 Given the spatial extent, timescale, and magnitude of the late 2016 and 2019 circumpolar  
397 surface warming anomalies, it is unlikely that these events signify a long-term shift in the South

398 Ocean climate. As the circumpolar westerlies continue to intensify and shift poleward, the upper  
399 overturning cell of the Southern Ocean is expected to strengthen, increasing the upwelling of warm  
400 Circumpolar Deep Water across the Antarctic sea ice zone (Ferreira et al. 2015; Kostov et al.  
401 2017). Additionally, stronger winds will likely energize eddies across the circumpolar channel that  
402 will partially negate the Ekman overturning response (Farneti et al. 2010; Doddridge et al. 2019).  
403 However, the warming rates associated with these adjustments to the Southern Ocean overturning  
404 circulation are expected to be orders of magnitude smaller than the anomalous surface warming  
405 observed during the austral spring of 2016 and 2019. Further, the recent circumpolar surface  
406 warming events spanned the ice-free regions of the Southern Ocean, where potential temperature  
407 decreases with depth below the seasonal pycnocline. However, there is evidence that interannual  
408 upper ocean upwelling trends contributed substantially to the prolonged period of below-average  
409 Antarctic SIE between 2016 and 2020 Meehl et al. (2019). The recent decline in Antarctic sea  
410 ice cover has been most pronounced in the Weddell Sea (Parkinson 2019), which featured large  
411 open-ocean polynyas and deep convection during the winters of 2016 and 2017 (Cheon and Gordon  
412 2019). These polynya events were facilitated by enhanced upwelling across the Weddell Gyre,  
413 which gradually eroded the local pycnocline and preconditioned the region for deep convection  
414 (Campbell et al. 2019). Thus, we surmise that the anomalous Southern Ocean surface warming  
415 and sea ice loss since 2016 were primarily due to a culmination of several climate processes acting  
416 over sub-seasonal to interannual timescales.

417 Additional work is needed to determine how the variability of SAM and its impacts on Southern  
418 Ocean MLD and SST will evolve under anthropogenic forcing. Previous studies have primarily  
419 focused on the mean-state ocean response to the ongoing trend toward a more positive SAM  
420 phase, in particular, the ocean overturning response to a strengthening and poleward shift of the  
421 circumpolar westerlies (e.g., Bitz and Polvani 2012; Ferreira et al. 2015; Kostov et al. 2017).  
422 However, our results demonstrate that near-surface processes acting on sub-seasonal timescales  
423 will set future surface warming extremes. The current positive trend in the SAM index is largest  
424 in austral summer (Fogt and Marshall 2020), which favors more vigorous wind-driven mixing and  
425 deeper mixed layers. On the other hand, current surface warming and freshening trends will induce  
426 stronger near-surface stratification and possibly shallower mixed layers. Over the past several  
427 decades, these competing processes have led to a deepening of the Southern Ocean mixed layer



428 and a concurrent enhancement of the stratification across the base of the mixed layer (Sallée et al.  
429 2021). The extent to which these trends persist will impact the frequency and intensity of future  
430 abrupt surface warming events and marine heatwaves in the Southern Ocean.

## 431 **5. Conclusions**

432 The abrupt Southern Ocean surface warming anomalies of late 2016 and 2019 were primarily  
433 the result of amplified air-sea heating and reduced northward Ekman transport. The former effect  
434 was due to an unusually early springtime shoaling of the Southern Ocean mixed layer. Both  
435 surface warming events were initiated by a collapse of the circumpolar westerlies associated with  
436 extreme negative SAM events. Equivalent warming events are found in the CESM1-LE, wherein  
437 the Southern Ocean SST and MLD response to SAM are consistent with recent observations.  
438 Therefore, it is plausible that recent Southern Ocean surface warming anomalies are purely the  
439 result of internal variability. Generalizing these recent circumpolar surface warming events, we  
440 show that interannual variability of summertime Southern Ocean SST is controlled by the variability  
441 of SAM in austral spring. Further, the amplitude of these warming events is modulated by the  
442 mean-state MLD, whereby deeper mixed layers favor more muted SST variability.

443 As the Southern Ocean climate evolves over the 21st century, the frequency and intensity of  
444 surface warming extremes will depend on the evolution of SAM, surface winds, and MLD. Though  
445 past studies have shown the current trend towards positive SAM will eventually lead to sustained  
446 surface warming across the Southern Ocean (Ferreira et al. 2015; Bitz and Polvani 2012), it is  
447 less clear how the interannual variability of SAM and summertime Southern Ocean SST will co-  
448 evolve. The Southern Ocean MLD is a critical bridge that links future Southern Ocean warming  
449 across decadal and interannual timescales, with shallower time-mean MLDs facilitating more  
450 extreme variations in SST. Projecting the evolution of Southern Ocean MLD is complicated by  
451 its dependence on competing processes: the projected strengthening of the circumpolar westerlies  
452 and increases in surface buoyancy fluxes via warming and enhanced freshwater fluxes (Meredith  
453 et al. 2019; Sallée et al. 2021). In a scenario where stronger winds dominate MLD trends,  
454 the Southern Ocean surface may experience steady decadal warming but reduced interannual  
455 variability due to a concurrent deepening of the mixed layer in spring and summer. Alternatively,  
456 if the surface mixed layer shoals over the coming decades, the region will likely experience more

457 intense surface warming extremes, which would exacerbate the impact of the expected time-mean  
458 surface warming trend. These extreme warming scenarios will have profound consequences for  
459 the viability of regional ecosystems and biogeochemical processes. Thus, it is critical to establish  
460 bounds on the temporal variance that may envelope future warming trends.

*Acknowledgments.* E.A.W. acknowledges support from Caltech’s Terrestrial Hazard Observations and Reporting Center. D.B.B. was supported by the National Science Foundation Graduate Research Fellowship Program (NSF Grant DGE-1745301). A.F.T. received support from NSF award OCE-1756956 and the Internal Research and Technology Development program (Earth 2050), Jet Propulsion Laboratory, California Institute of Technology. E.A.W. and S.C.R. received support through the SOCCOM Project, funded by the National Science Foundation, Division of Polar Programs (NSF PLR-1425989 and OPP-1936222). E.A.W. and S.C.R. also received funding from NOAA as part of the US Argo Program via grant NA20OAR4320271 to the University of Washington.

*Data availability statement.* All data and reanalysis products used in this study are sourced from publicly accessible repositories. NOAA Optimum Interpolation SST V2 data were retrieved from <https://psl.noaa.gov/data/gridded/data.noaa.oisst.v2.html>. The Roemmich-Gilson Argo product was downloaded from [https://sio-argo.ucsd.edu/RG\\_Climatology.html](https://sio-argo.ucsd.edu/RG_Climatology.html). ERA5 reanalysis can be accessed at <https://doi.org/10.24381/cds.f17050d7>. Model output from the CESM1-LE can be downloaded from <https://www.cesm.ucar.edu/projects/community-projects/LENS/data-sets.html>. NOAA/NSIDC Climate Data Record of Passive Microwave Sea Ice Concentration (Version 4) can be accessed at <https://doi.org/10.7265/efmz-2t65z>. Python code for carrying out analysis and generating figures is available at <https://doi.org/10.5281/zenodo.6588645>.

## APPENDIX

### **A1. Ensemble experiments with a 1D mixing model**

To evaluate the impact of wind perturbations on MLT warming, we use a modified version of the Kraus-Turner 1D upper ocean mixing model (Kraus and Turner 1967; Niiler 1975; Niiler and Kraus 1977). This bulk mixed layer model simulates the evolution of the surface mixed layer by balancing the stabilizing effect of surface buoyancy fluxes (i.e., the addition of heat or freshwater to the water column) and the destabilizing effect of wind-driven mixing. Variants of the Kraus-Turner model have been used extensively to study surface mixed layer variations over a wide range of settings, including in subpolar regions (Biddle et al. 2017). Following Chen et al. (1994), the entrainment

489 rate,  $w_{ent}$ , of the mixed layer is given by

$$490 \quad w_{ent} = \frac{P_w - P_b}{h_m \Delta b}, \quad (A1)$$

491 where  $\Delta b$  is the buoyancy difference across the base of the mixed layer, and  $P_w$  and  $P_b$  are work  
 492 provided by surface wind stress and the potential energy supplied by surface buoyancy fluxes,  
 493 respectively.  $P_w$  and  $P_b$  are given by

$$494 \quad P_w = 2\gamma_1 u_*^3, \quad (A2)$$

$$495 \quad P_b = \frac{h_m}{2} [(1 + \gamma_2) B_0 - (1 - \gamma_2) |B_0|], \quad (A3)$$

497 where  $\gamma_1 = 0.4$  and  $\gamma_2 = 0.18$  are empirically derived mixing coefficients,  $u_*$  is the friction velocity,  
 498 and  $B_0$  is the total surface buoyancy flux. The above formulation is valid for a stably stratified  
 499 water column ( $\Delta b > 0$ ). For scenarios where  $P_w - P_b > 0$ , the mixed layer deepens and (A1) is  
 500 used to determine the entrainment rate. For cases of mixed layer shoaling, we assume  $P_w$  and  $P_b$   
 501 are in balance and we use the relationships (A2) and (A3) to determine  $h_m$ .

502 The mixing model is initialized with idealized temperature and salinity profiles representative  
 503 of the circumpolar channel between 50°–65°S in early October. At the start of each simulation,  
 504 the mixed layer depth is set to 125 m, and temperature and salinity in the mixed layer are set  
 505 to 1 °C and 33.4 PSU, respectively. Below the mixed layer, there is a 150 m thick seasonal  
 506 pycnocline, across which temperature and salinity linearly transition to fixed values of 0°C and  
 507 ~33.6 PSU, respectively. We prescribe a surface heat flux that approximates the climatological  
 508 net surface heating across the circumpolar channel between October and March (150 days total).  
 509 To isolate the impact of surface winds and heating, we impose a constant surface freshwater flux  
 510 (i.e., precipitation minus evaporation) of 1 mm day<sup>-1</sup>. The buoyancy forcing is combined with a  
 511 synthetically generated surface wind stress  $\tau$ , which is modeled as the sum of a red-noise sequence  
 512  $\hat{\tau}(t)$  and a mean offset  $\bar{\tau}$ :

$$513 \quad \tau(t) = \hat{\tau}(t) + \bar{\tau}, \quad (A4)$$

$$514 \quad \hat{\tau}(t) = a \hat{\tau}(t - \Delta t) + \sqrt{(1 - a^2)} \epsilon(t), \quad (A5)$$

515

where  $a = 0.9$  is the lag-1 auto-correlation coefficient,  $\Delta t = 6$  hours is the time step,  $\epsilon$  is a randomly generated white noise sequence with a standard deviation of 0.05, and  $\bar{\tau} = 0.1 \text{ N m}^{-2}$ . The numerical model is evolved with a vertical resolution of 0.25 m and a 6 hourly time step. A total of six ensemble experiments are carried out: one control experiment consisting of 200 independent simulations, each with a unique wind forcing, and five perturbation experiments wherein  $\bar{\tau}$  is reduced over different time windows, centered on days 15, 45, 75, 105, and 135 (after October 1). For the perturbation experiments, the magnitude of the time-mean wind stress is reduced by a maximum of 50% using a Gaussian window with a standard deviation of 5 days. By perturbing  $\bar{\tau}$  in Equation (A5), the temporal variance of  $\tau$  is preserved.

## References

- Armour, K. C., J. Marshall, J. R. Scott, A. Donohoe, and E. R. Newsom, 2016: Southern Ocean warming delayed by circumpolar upwelling and equatorward transport. *Nature Geoscience*, **9** (7), 549–554, <https://doi.org/10.1038/ngeo2731>.
- Biddle, L. C., K. J. Heywood, J. Kaiser, and A. Jenkins, 2017: Glacial meltwater identification in the Amundsen Sea. *Journal of Physical Oceanography*, JPO–D–16–0221.1, <https://doi.org/10.1175/JPO-D-16-0221.1>.
- Bintanja, R., G. J. V. Oldenborgh, S. S. Drijfhout, B. Wouters, and C. A. Katsman, 2013: Important role for ocean warming and increased ice-shelf melt in Antarctic sea-ice expansion. *Nature Geoscience*, **6** (5), 376–379, <https://doi.org/10.1038/ngeo1767>.
- Bitz, C. M., and L. M. Polvani, 2012: Antarctic climate response to stratospheric ozone depletion in a fine resolution ocean climate model. *Geophysical Research Letters*, **39** (20), <https://doi.org/10.1029/2012GL053393>.
- Campbell, E. C., E. A. Wilson, G. W. Moore, S. C. Riser, C. E. Brayton, M. R. Mazloff, and L. D. Talley, 2019: Antarctic offshore polynyas linked to Southern Hemisphere climate anomalies. *Nature*, **570** (7761), 319–325, <https://doi.org/10.1038/s41586-019-1294-0>.
- Carranza, M. M., and S. T. Gille, 2015: Southern Ocean wind-driven entrainment enhances satellite chlorophyll-a through the summer. *Journal of Geophysical Research: Oceans*, **120** (1), 304–323, <https://doi.org/10.1002/2014JC010203>.

544 Cavalieri, D. J., C. L. Parkinson, and K. Y. Vinnikov, 2003: 30-year satellite record reveals  
 545 contrasting Arctic and Antarctic decadal sea ice variability. *Geophysical Research Letters*,  
 546 **30 (18)**, <https://doi.org/10.1029/2003GL018031>.

547 Chen, D., L. M. Rothstein, and A. J. Busalacchi, 1994: A Hybrid Vertical Mixing Scheme and Its  
 548 Application to Tropical Ocean Models. *Journal of Physical Oceanography*, **24 (10)**, 2156–2179,  
 549 [https://doi.org/10.1175/1520-0485\(1994\)024<2156:AHVMSA>2.0.CO;2](https://doi.org/10.1175/1520-0485(1994)024<2156:AHVMSA>2.0.CO;2).

550 Cheon, W. G., and A. L. Gordon, 2019: Open-ocean polynyas and deep convection in the Southern  
 551 Ocean. *Scientific Reports*, **9 (1)**, 6935, <https://doi.org/10.1038/s41598-019-43466-2>.

552 Chung, E.-S., and Coauthors, 2022: Antarctic sea-ice expansion and Southern Ocean cooling linked  
 553 to tropical variability. *Nature Climate Change*, <https://doi.org/10.1038/s41558-022-01339-z>.

554 Ciasto, L. M., and M. H. England, 2011: Observed ENSO teleconnections to Southern Ocean SST  
 555 anomalies diagnosed from a surface mixed layer heat budget. *Geophysical Research Letters*,  
 556 **38 (9)**, <https://doi.org/10.1029/2011GL046895>.

557 de Boyer Montégut, C., G. Madec, A. S. Fischer, A. Lazar, and D. Iudicone, 2004: Mixed layer depth  
 558 over the global ocean: An examination of profile data and a profile-based climatology. *Journal*  
 559 *of Geophysical Research C: Oceans*, **109 (12)**, 1–20, <https://doi.org/10.1029/2004JC002378>.

560 Ding, Q., E. J. Steig, D. S. Battisti, and J. M. Wallace, 2012: Influence of the tropics  
 561 on the southern annular mode. *Journal of Climate*, **25 (18)**, 6330–6348, <https://doi.org/10.1175/JCLI-D-11-00523.1>.

562

563 Doddridge, E. W., J. Marshall, H. Song, J. M. Campin, M. Kelley, and L. Nazarenko,  
 564 2019: Eddy Compensation Dampens Southern Ocean Sea Surface Temperature Response  
 565 to Westerly Wind Trends. *Geophysical Research Letters*, **46 (8)**, 4365–4377, <https://doi.org/10.1029/2019GL082758>.

566

567 Dong, S., S. T. Gille, and J. Sprintall, 2007: An assessment of the Southern Ocean mixed layer  
 568 heat budget. *Journal of Climate*, **20 (17)**, 4425–4442, <https://doi.org/10.1175/JCLI4259.1>.

569 Dong, S., J. Sprintall, S. T. Gille, and L. Talley, 2008: Southern ocean mixed-layer depth from  
 570 Argo float profiles. *Journal of Geophysical Research: Oceans*, **113 (6)**, <https://doi.org/10.1029/2006JC004051>.

571

du Plessis, M., S. Swart, L. C. Biddle, I. S. Giddy, P. M. S. Monteiro, C. J. C. Reason, A. F. Thompson, and S. Nicholson, 2022: The Daily-Resolved Southern Ocean Mixed Layer: Regional Contrasts Assessed Using Glider Observations. *Journal of Geophysical Research: Oceans*, **127** (4), <https://doi.org/10.1029/2021JC017760>.

Eayrs, C., X. Li, M. N. Raphael, and D. M. Holland, 2021: Rapid decline in Antarctic sea ice in recent years hints at future change. *Nature Geoscience*, **14** (7), 460–464, <https://doi.org/10.1038/s41561-021-00768-3>.

Fan, T., C. Deser, and D. P. Schneider, 2014: Recent Antarctic sea ice trends in the context of Southern Ocean surface climate variations since 1950. *Geophysical Research Letters*, **41** (7), 2419–2426, <https://doi.org/10.1002/2014GL059239>.

Farneti, R., T. L. Delworth, A. J. Rosati, S. M. Griffies, and F. Zeng, 2010: The role of mesoscale eddies in the rectification of the Southern ocean response to climate change. *Journal of Physical Oceanography*, **40** (7), 1539–1557, <https://doi.org/10.1175/2010JPO4353.1>.

Ferreira, D., J. Marshall, C. M. Bitz, S. Solomon, and A. Plumb, 2015: Antarctic ocean and sea ice response to ozone depletion: A two-time-scale problem. *Journal of Climate*, **28** (3), 1206–1226, <https://doi.org/10.1175/JCLI-D-14-00313.1>.

Fogt, R. L., and G. J. Marshall, 2020: The Southern Annular Mode: Variability, trends, and climate impacts across the Southern Hemisphere. *WIREs Climate Change*, **11** (4), <https://doi.org/10.1002/wcc.652>.

Frölicher, T. L., E. M. Fischer, and N. Gruber, 2018: Marine heatwaves under global warming. *Nature*, **560** (7718), 360–364, <https://doi.org/10.1038/s41586-018-0383-9>.

Gao, Y., I. Kamenkovich, N. Perlin, and B. Kirtman, 2022: Oceanic Advection Controls Mesoscale Mixed Layer Heat Budget and Air–Sea Heat Exchange in the Southern Ocean. *Journal of Physical Oceanography*, **52** (4), 537–555, <https://doi.org/10.1175/JPO-D-21-0063.1>.

Haumann, F. A., N. Gruber, and M. Münnich, 2020: Sea-Ice Induced Southern Ocean Subsurface Warming and Surface Cooling in a Warming Climate. *AGU Advances*, **1** (2), <https://doi.org/10.1029/2019AV000132>.

Hersbach, H., and Coauthors, 2020: The ERA5 global reanalysis. *Quarterly Journal of the Royal Meteorological Society*, **146** (730), 1999–2049, <https://doi.org/10.1002/qj.3803>.

Hobday, A. J., and Coauthors, 2016: A hierarchical approach to defining marine heatwaves. *Progress in Oceanography*, **141**, 227–238, <https://doi.org/10.1016/j.pocean.2015.12.014>.

Holbrook, N. J., and Coauthors, 2019: A global assessment of marine heatwaves and their drivers. *Nature Communications*, **10** (1), 2624, <https://doi.org/10.1038/s41467-019-10206-z>.

Kay, J. E., and Coauthors, 2015: The Community Earth System Model (CESM) Large Ensemble Project: A Community Resource for Studying Climate Change in the Presence of Internal Climate Variability. *Bulletin of the American Meteorological Society*, **96** (8), 1333–1349, <https://doi.org/10.1175/BAMS-D-13-00255.1>.

Kostov, Y., J. Marshall, U. Hausmann, K. C. Armour, D. Ferreira, and M. M. Holland, 2017: Fast and slow responses of Southern Ocean sea surface temperature to SAM in coupled climate models. *Climate Dynamics*, **48** (5-6), 1595–1609, <https://doi.org/10.1007/s00382-016-3162-z>.

Kraus, E. B., and J. S. Turner, 1967: A one-dimensional model of the seasonal thermocline II. The general theory and its consequences. *Tellus*, **19** (1), 98–106, <https://doi.org/10.3402/tellusa.v19i1.9753>.

Li, X., and Coauthors, 2021: Tropical teleconnection impacts on Antarctic climate changes. *Nature Reviews Earth & Environment*, **2** (10), 680–698, <https://doi.org/10.1038/s43017-021-00204-5>.

Marshall, G. J., 2003: Trends in the Southern Annular Mode from observations and reanalyses. *Journal of Climate*, **16** (24), 4134–4143, [https://doi.org/10.1175/1520-0442\(2003\)016<4134:TITSAM>2.0.CO;2](https://doi.org/10.1175/1520-0442(2003)016<4134:TITSAM>2.0.CO;2).

Meehl, G. A., J. M. Arblaster, C. M. Bitz, C. T. Y. Chung, and H. Teng, 2016: Antarctic sea-ice expansion between 2000 and 2014 driven by tropical Pacific decadal climate variability. *Nature Geoscience*, **9** (8), 590–595, <https://doi.org/10.1038/ngeo2751>.

Meehl, G. A., J. M. Arblaster, C. T. Y. Chung, M. M. Holland, A. DuVivier, L. A. Thompson, D. Yang, and C. M. Bitz, 2019: Sustained ocean changes contributed to sudden Antarctic sea ice retreat in late 2016. *Nature Communications*, **10** (1), <https://doi.org/10.1038/s41467-018-07865-9>.



Meier, W., F. Fetterer, M. Savoie, S. Mallory, R. Duerr, and J. Stroeve, 2013: NOAA/NSIDC Climate Data Record of Passive Microwave Sea Ice Concentration. NSIDC: National Snow and Ice Data Center, <https://doi.org/10.7265/N59P2ZTG>.

Meredith, M., and Coauthors, 2019: Polar Regions. *Ocean Cryosph. a Chang. Clim.*, H.-O. Pörtner, D. C. Roberts, V. Masson-Delmotte, P. Zhai, M. Tignor, E. Poloczanska, K. Mintenbeck, A. Alegría, M. Nicolai, A. Okem, J. Petzold, B. Rama, and N. M. Weyer, Eds., Cambridge University Press, Cambridge, chap. 3, 203–320, <https://doi.org/10.1017/9781009157964.005>.

Niiler, P. P., 1975: The deepening of the wind-mixed layer. *Journal of Marine Research*, **33** (3), 405–422.

Niiler, P. P., and E. B. Kraus, 1977: One Dimensional Models of the Upper Ocean. Pergamon, 143–172 pp.

Oliver, E. C. J., J. A. Benthuisen, S. Darmaraki, M. G. Donat, A. J. Hobday, N. J. Holbrook, R. W. Schlegel, and A. S. Gupta, 2021: Marine Heatwaves. *Annual Review of Marine Science*, **13** (1), 313–342, <https://doi.org/10.1146/annurev-marine-032720-095144>.

Parkinson, C. L., 2019: A 40-y record reveals gradual Antarctic sea ice increases followed by decreases at rates far exceeding the rates seen in the Arctic. *Proceedings of the National Academy of Sciences*, **116** (29), 14 414–14 423, <https://doi.org/10.1073/pnas.1906556116>.

Pellichero, V., J. B. Sallée, S. Schmidtke, F. Roquet, and J. B. Charrassin, 2017: The ocean mixed layer under Southern Ocean sea-ice: Seasonal cycle and forcing. *Journal of Geophysical Research: Oceans*, **122** (2), 1608–1633, <https://doi.org/10.1002/2016JC011970>.

Purich, A., and M. H. England, 2019: Tropical Teleconnections to Antarctic Sea Ice During Austral Spring 2016 in Coupled Pacemaker Experiments. *Geophysical Research Letters*, **46** (12), 6848–6858, <https://doi.org/10.1029/2019GL082671>.

Purich, A., M. H. England, W. Cai, A. Sullivan, and P. J. Durack, 2018: Impacts of broad-scale surface freshening of the Southern Ocean in a coupled climate model. *Journal of Climate*, **31** (7), 2613–2632, <https://doi.org/10.1175/JCLI-D-17-0092.1>.

653 Rackow, T., S. Danilov, H. F. Goessling, H. H. Hellmer, D. V. Sein, T. Semmler, D. Sidorenko, and  
654 T. Jung, 2022: Delayed Antarctic sea-ice decline in high-resolution climate change simulations.  
655 *Nature Communications*, **13** (1), 637, <https://doi.org/10.1038/s41467-022-28259-y>.

656 Reynolds, R. W., N. A. Rayner, T. M. Smith, D. C. Stokes, and W. Wang, 2002: An improved in situ  
657 and satellite SST analysis for climate. *Journal of Climate*, **15** (13), 1609–1625, [https://doi.org/10.1175/1520-0442\(2002\)015<1609:AIISAS>2.0.CO;2](https://doi.org/10.1175/1520-0442(2002)015<1609:AIISAS>2.0.CO;2).

658  
659 Roemmich, D., and J. Gilson, 2009: The 2004–2008 mean and annual cycle of temperature, salinity,  
660 and steric height in the global ocean from the Argo Program. *Progress in Oceanography*, **82** (2),  
661 81–100, <https://doi.org/10.1016/j.pocean.2009.03.004>.

662 Sallée, J. B., K. G. Speer, and S. R. Rintoul, 2010: Zonally asymmetric response of the Southern  
663 Ocean mixed-layer depth to the Southern Annular Mode. *Nature Geoscience*, **3** (4), 273–279,  
664 <https://doi.org/10.1038/ngeo812>.

665 Sallée, J.-B., and Coauthors, 2021: Summertime increases in upper-ocean stratification and mixed-  
666 layer depth. *Nature*, **591** (7851), 592–598, <https://doi.org/10.1038/s41586-021-03303-x>.

667 Schlosser, E., F. A. Haumann, and M. N. Raphael, 2018: Atmospheric influences on the  
668 anomalous 2016 Antarctic sea ice decay. *Cryosphere*, **12** (3), 1103–1119, <https://doi.org/10.5194/tc-12-1103-2018>.

669  
670 Sen Gupta, A., and M. H. England, 2006: Coupled ocean-atmosphere-ice response to variations in  
671 the southern annular mode. *J. Clim.*, **19** (18), 4457–4486, <https://doi.org/10.1175/JCLI3843.1>.

672 Simmonds, I., 2015: Comparing and contrasting the behaviour of Arctic and Antarctic sea ice  
673 over the 35 year period 1979–2013. *Annals of Glaciology*, **56** (69), 18–28, <https://doi.org/10.3189/2015AoG69A909>.

674  
675 Smale, D. A., and Coauthors, 2019: Marine heatwaves threaten global biodiversity and the  
676 provision of ecosystem services. *Nature Climate Change*, **9** (4), 306–312, <https://doi.org/10.1038/s41558-019-0412-1>.

677  
678 Stuecker, M. F., C. M. Bitz, and K. C. Armour, 2017: Conditions leading to the unprecedented low  
679 Antarctic sea ice extent during the 2016 austral spring season. *Geophysical Research Letters*,  
680 **44** (17), 9008–9019, <https://doi.org/10.1002/2017GL074691>.

681 Tamsitt, V., L. D. Talley, M. R. Mazloff, and I. Cerovecki, 2016: Zonal variations in  
682 the Southern Ocean heat budget. *Journal of Climate*, **29** (18), 6563–6579, [https://doi.org/](https://doi.org/10.1175/JCLI-D-15-0630.1)  
683 10.1175/JCLI-D-15-0630.1.

684 Turner, J., T. Phillips, G. J. Marshall, J. S. Hosking, J. O. Pope, T. J. Bracegirdle, and P. Deb, 2017:  
685 Unprecedented springtime retreat of Antarctic sea ice in 2016. *Geophysical Research Letters*,  
686 **44** (13), 6868–6875, <https://doi.org/10.1002/2017GL073656>.

687 Wang, G., H. H. Hendon, J. M. Arblaster, E. P. Lim, S. Abhik, and P. van Rensch, 2019: Com-  
688 pounding tropical and stratospheric forcing of the record low Antarctic sea-ice in 2016. *Nature*  
689 *Communications*, **10** (1), 13, <https://doi.org/10.1038/s41467-018-07689-7>.

690 Yuan, X., and D. G. Martinson, 2000: Antarctic sea ice extent variability and its global connectivity.  
691 *Journal of Climate*, **13** (10), 1697–1717, [https://doi.org/10.1175/1520-0442\(2000\)013<1697:](https://doi.org/10.1175/1520-0442(2000)013<1697:ASIEVA>2.0.CO;2)  
692 ASIEVA>2.0.CO;2.

693 Zhang, L., T. L. Delworth, W. Cooke, and X. Yang, 2019: Natural variability of Southern  
694 Ocean convection as a driver of observed climate trends. *Nature Climate Change*, **9** (1), 59–65,  
695 <https://doi.org/10.1038/s41558-018-0350-3>.